An Upper Limit to [C II] Emission in a $z \simeq 5$ Galaxy

by

Anthony Gaelen Marsden

B.Sc., The University of British Columbia, 2000

A THESIS SUBMITTED IN PARTIAL FULFILMENT OF
THE REQUIREMENTS FOR THE DEGREE OF

MASTER OF SCIENCE

in

The Faculty of Graduate Studies

(Department of Physics and Astronomy)

We accept this thesis as conforming
to the required standard

.....

.....

THE UNIVERSITY OF BRITISH COLUMBIA

October 7, 2002

In presenting this thesis in partial fulfilment of the requirements for an advanced degree at the University of British Columbia, I agree that the Library shall make it freely available for reference and study. I further agree that permission for extensive copying of this thesis for scholarly purposes may be granted by the head of my department or by his or her representatives. It is understood that copying or publication of this thesis for financial gain shall not be allowed without my written permission.

(Signature) _____

Department of Physics and Astronomy

The University Of British Columbia
Vancouver, Canada

Date _____

Abstract

Low ionization state far-IR emission lines play an important role in cooling star-forming regions, as they are an unambiguous link between UV and IR photons. Star-forming galaxies have large dust masses which obscure UV radiation, so we rely on the IR to probe these star-forming regions. Such lines may be useful diagnostics of star-formation activity in young galaxies, and at high redshift may be detectable from the ground. In practice, however, very little is known about how strong this line emission might be in the early universe. We attempted to detect the 158 μm [C II] line from a lensed galaxy at $z = 4.92$ using the Caltech Submillimeter Observatory. This source is an ordinary galaxy, in the sense that it does not show extreme star formation, but lensing makes it visible. Our analysis includes a careful consideration of the calibrations and weighting of the individual scans. We find only modest improvement over the simpler reduction methods, however, and the final spectrum remains dominated by systematic baseline ripple effects. We obtain a 95% confidence upper limit of 33 mJy for a 200 km s^{-1} FWHM line, corresponding to an unlensed magnitude of 1×10^9 L$_\odot$ for a standard cosmological model. Combining this with a marginal detection of the continuum emission using the James Clerk Maxwell Telescope, we can derive an upper limit of 0.4% for the ratio of $L_{[\mathrm{C\,II}]}/L_{\mathrm{FIR}}$.

Contents

List of Tables

List of Figures

Acknowledgements

I would like to thank Mark Halpern and Douglas Scott for their continual help through the life of this project. Thanks also to Colin Borys and Scott Chapman for their assistance with the reduction of the SCUBA data. And finally, thanks to the Natural Sciences and Engineering Research Council of Canada, without whom my studies would not be possible.

Chapter 1

[C II] in High-redshift Galaxies

Galaxy formation and evolution is poorly understood; the physics is very complicated. We therefore rely on empirical studies to piece together the history of the Universe we see today. Current star formation rates (SFRs) are too low to account for the stellar masses and metallicities seen in low redshift galaxies, suggesting that SFRs must have been higher in the past. Observations of the cosmic microwave background (CMB) at $z \gtrsim 1000$, however, show only weak fluctuations that may evolve into galaxies [45]. Thus, galaxies formed and had relatively high SFRs at some time between $z \sim 1000$ and $z \sim 1$ [39]. Cold dark matter (CDM) models predict that SFR peaks at $z \sim 2$, which appears to be confirmed by observations. The low number of known high redshift sources, though, means that SFR as a function of lookback time is still relatively unknown. Finding high redshift galaxies in an unbiased manner is therefore a priority in modern observational cosmology.

Researchers have had great success finding $z \gtrsim 3$ galaxies by searching for redshifted Ly α emission and the Lyman break in the spectrum (see the review by Giavalisco [17]). Galaxies found this way may be a biased sample, though; star-bursting galaxies produce dust which obscures the ultraviolet (UV) radiation. At longer wavelengths, however, extinction is much less of a problem. Stellar UV radiation heats the dusty regions surrounding the star, and re-emits in the far-infrared (FIR). FIR continuum and emission lines can be used to probe the star-formation in the source galaxy. In particular, the ground state fine structure line of singly ionized carbon, called [C II], has been shown to be the dominant cooling line in gas-rich star-forming regions [9, 10, 38]. It is the transition from $^2P_{3/2}$ to $^2P_{1/2}$ and has a rest wavelength of $\lambda = 157.7409\,\mu$m.

It is thought that the majority of [C II] emission is produced in photodissociation regions (PDRs), the interface between the hot H II regions surrounding young stars

and the cooler surrounding molecular clouds [9, 18, 21, 28, 42, 46]. Here, UV photons with energy less than the hydrogen ionization energy of 13.6 eV, which have passed right through the H II regions, dissociate molecules and ionize neutral elements in the first layer of the molecular clouds. The ions are then excited by photo-electrons emitted by dust grains and polycyclic aromatic hydrocarbons (PAHs) submitted to UV radiation from the young stars. Carbon is the most abundant element with ionization potential < 13.6 eV (11.26 eV), and thus C^+, the de-excitation of which produces the [C II] emission, is expected to be the most common ion in PDRs. Additionally, [C II] has a low excitation energy ($\Delta E/k \simeq 91$ K), so it is easily excited in the warm PDRs. PDRs are transparent at 158 μm so heat is transported away. For these reasons, [C II] is thought to be a significant cooling line in galaxies.

Many efforts have been made to detect [C II] emission, and to determine the ratio of [C II] luminosity to FIR luminosity, $L_{[\mathrm{C\,II}]}/L_{\mathrm{FIR}}$. This includes studies of the Milky Way, star-forming galaxies and ultraluminous infrared galaxies (ULIRGs) in the nearby universe, and young star-forming galaxies in the high redshift universe. [C II] is redshifted to atmospheric windows in the submillimetre for sources at $z \sim 2 - 6$.

Many groups have looked for and detected [C II] in the Galaxy. Wright et al. describe observations with the far-infrared absolute spectrophotometer (FIRAS) on the Cosmic Background Explorer (COBE) [48]. They detected [C II] at all Galactic longitudes and latitudes, and found that it has a spatial distribution similar to the dust distribution. They concluded that [C II] is the brightest FIR line in the Galaxy, with $L_{[\mathrm{C\,II}]}/L_{\mathrm{FIR}} \simeq 0.3\%$. Mizutani et al. observed the Galactic centre with the Balloon-borne Infrared Telescope (BIRT) [31]. They discovered that the [C II] emission is morphologically associated with H II regions and molecular clouds, supporting the view that [C II] is produced in PDRs. They find $L_{[\mathrm{C\,II}]}/L_{\mathrm{FIR}} \sim 0.06\%$ in that region, and suggest the low level may be due to excessive UV radiation, as seen in the active H II regions in the observed area.

Crawford et al. were the first to detect [C II] in extragalactic objects [9]. They used the Kuiper Airborne Observatory (KAO) to observe 6 gas-rich IR-bright galaxies, and detected the emission line at a level of $L_{[\mathrm{C\,II}]}/L_{\mathrm{FIR}} \sim 0.2\%$. A few years

later, Stacey et al. (hereafter S91) extended the sample to include (i) a wider range of luminosity classes in IR bright galaxies, and (ii) a wide spectral range of spiral galaxies not noted for excessive star formation, also using the KAO [38]. They detected [C II] in 11 of the 13 galaxies studied and concluded that $L_{[\mathrm{C\,II}]}/L_{\mathrm{FIR}}$ ranges from 0.1 to 1%, with no clear dependence on galactic spectral type. Nikola et al. observed the interacting galaxies NGC 4038/9 (the "Antennae") using the Far-infrared Imaging Fabry-Perot Interferometer (FIFI) on the KAO and found $L_{[\mathrm{C\,II}]}/L_{\mathrm{FIR}} \sim 1\%$ [33]. Similarly, Mochizuki looked at the central regions of M31 with the Long Wavelength Spectrometer (LWS) on the Infrared Space Telescope (ISO) and found $L_{[\mathrm{C\,II}]}/L_{\mathrm{FIR}} \sim 0.6\%$ [32]. Leech et al. observed a sample of 15 Virgo cluster spirals with quiescent star formation using ISO/LWS [24]. They find $L_{[\mathrm{C\,II}]}/L_{\mathrm{FIR}} \sim 0.1 - 0.5\%$ for their sample.

For many years, it seemed quite clear that $L_{[\mathrm{C\,II}]}/L_{\mathrm{FIR}} \sim 0.1 - 1\%$ in nearby ULIRGs and high redshift gas-rich star-bursting galaxies [15]. More recently, however, studies have shown that [C II] may sometimes be weaker than originally thought. Malhotra et al. observed 30 normal nearby star-forming galaxies with ISO/LWS [29]. They found $L_{[\mathrm{C\,II}]}/L_{\mathrm{FIR}} \sim 0.2 - 0.7\%$ for two-thirds of their sample, but $< 0.1\%$ for the warmer, more actively star-forming galaxies. [C II] was undetected at the 3σ level of $L_{[\mathrm{C\,II}]}/L_{\mathrm{FIR}} < 0.5 - 5 \times 10^{-4}$ for 3 of the 30 sources in their sample. Similarly, Luhman et al. studied 7 ULIRGs, also using the LWS, and found $L_{[\mathrm{C\,II}]}/L_{\mathrm{FIR}} < 5 \times 10^{-4}$ [26]. Contursi et al. looked at the nearby spirals NGC 6946 and NGC 1313 with ISO/LWS and found $L_{[\mathrm{C\,II}]}/L_{\mathrm{FIR}} \simeq 0.8\%$ [8]. They used the Kaufman et al. PDR model [21] to derive physical parameters responsible for the neutral atomic gas, and concluded that their results do not differ significantly from Malhotra et al. Several possible explanations for the deficit are provided:

- For high UV flux to gas density ($G_0/n \gtrsim 10\,\mathrm{cm}^3$) the dust grains are positively charged and are less efficient at heating gas. [C II] also becomes saturated at high G_0/n.
- For large densities, C^+ ions can become collisionally de-excited.
- FIR continuum emission could come from H II regions and diffuse atomic

clouds, as well as from PDRs, which would have lower $L_{[\mathrm{C\,II}]}/L_{\mathrm{FIR}}$ ratios.

- Compact FIR sources, for example a buried AGN, could produce a lot of FIR without much [C II], since the hard UV emitted by the AGN would be inefficient at making [C II].
- Conversely, a soft UV field, due to an aging starburst of an initial mass function with a low upper mass cutoff, would produce low $L_{[\mathrm{C\,II}]}/L_{\mathrm{FIR}}$.
- [C II] might be optically thick or self absorbed.

Boselli et al. propose, based on ISO/LWS observations [24, 36], that since massive galaxies form less stars per unit mass, early-type spirals have lower normalized [C II] emission than late-type spirals [3]. They conclude that [C II] can be used as an indicator of star formation in normal late-type spirals, but not in ULIRGs.

Because the submillimetre population of high redshift galaxies certainly contains some ULIRGs [15, 26], there is currently less optimism that [C II] will in fact be easily detectable in the high redshift universe. To date no detections of [C II] at high redshift have been made, although there have been many attempts. In one example, Soifer observed the IRAS object FSC 10214+4724, a gravitationally lensed ULIRG at $z = 2.286$ with the KAO [37], but did not detect [C II]. Ivison et al. [20] looked at a $z = 3.137$ damped Lyman-α system with reported CO emission [16], indicating rapid star formation. The CO detection was later shown to be spurious, however [4]. Ivison et al. did not detect the [C II] emission line in this system. The dusty $z = 4.693$ quasar BR 1202-0725 was observed from the James Clerk Maxwell Telescope (JCMT) [19, 43]. [C II] was also not detected for this object, and the authors quote an upper limit of $L_{[\mathrm{C\,II}]}/L_{\mathrm{FIR}} < 6 \times 10^{-4}$.

Although it may now appear that high redshift [C II] is not as easily detectable as previously thought, it still remains a bright line and is worth searching for in star-forming galaxies. We take advantage of the serendipitous discovery by Franx et al., hereafter referred to as F97, of a spectroscopically determined $z = 4.92$ galaxy lensed by the cluster CL 1358+62 [14]. This is one of the highest redshift known star forming galaxies, and at high enough redshift that [C II] is shifted into a relatively transparent frequency window. A lensed galaxy makes a reasonable target since

the magnified luminosity is easier to detect than for a similar unlensed galaxy. We observed the red arc, referred to as 'G1' by F97, using the Caltech Submillimeter Observatory (CSO) on Mauna Kea in Hawaii to see if we could detect [C II] emission.

This thesis is a presentation of these efforts. The observations are described in Chapter 2. Chapter 3 gives a detailed description of the data reduction process, and Chapter 4 presents the results. Chapter 5 is a discussion of how these results compare to others, and briefly describes how upcoming technology advances may benefit this field.

Chapter 2

Observations

The $z = 4.9218$ galaxy G1 was observed from the CSO over 3 nights in January 1998 by Scott Chapman, Mark Halpern, and Douglas Scott. The [C II] emission line has a rest-frame wavelength $\lambda = 157.7409\,\mu$m, which is redshifted to $\lambda_0 = \lambda(1+z)$, or $\nu_0 = 320.939$ GHz, for our source. We therefore use the CSO's 345 GHz receiver.

2.1 The telescope

The Caltech Submillimeter Observatory is located at 13,300 feet on the summit of Mauna Kea in Hawaii. It is a 10.4 metre f/0.4 submillimetre antenna with an alt-az mount. The secondary mirror chops in azimuth. The chop throw and frequency are set by the user, and the servo parameters can be tuned to achieve as high a duty cycle as possible.

The receiver is a single side-band SIS mixer with 1 GHz IF, and Acousto-optical Spectrometer (AOS) backends. The local oscillator mode is chosen and tuned by hand. For our observations the signals from the mixer were sent to 3 spectrometers simultaneously, with 50, 500, and 1500 MHz bandwidths. Note that the 1500 MHz backend is wider than the input intermediate band.

Temperature calibrations are performed frequently during the observation session. This is done by switching an ambient temperature "hot load" into the beam. First, the telescope is stepped off the source, and an attenuator is adjusted to protect the AOSs from the bright load. Then a chopper wheel inserts the hot load into the beam and data are taken. The load is then switched out of the beam and data are taken of the sky. Finally, the telescope is stepped back to the source and the

attenuator is re-adjusted. The calibration spectra are calculated as

$$\frac{\mathrm{HOT} - \mathrm{SKY}}{T_{\mathrm{amb}}}, \tag{2.1}$$

where T_{amb} is an assumed ambient temperature; the calibration spectra have units of *Volts per Kelvin.*

Frequency calibrations are performed whenever an AOS is started or restarted, and during long slews. The AOSs are thermally loaded, producing 5 spikes which allow the user to precisely determine each AOS's centre channel, total frequency coverage, and spectral resolution.

Pointing calibrations are meant to be performed several times each night. This involves pointing at a bright line source in a five-point pattern, with the offset distance set by the user (typically $\sim 10''$, half the telescope's beam width). A Gaussian is fit to the resulting brightness map to estimate the source's true centre. This procedure can be iterated until the user is satisfied that they have found the true centre.

Throughout the rest of this report, "calibration scan" refers to the temperature calibrations — spectra of the hot load — and "source scan" refers to spectra of our source, G1.

2.2 Atmospheric transmission

The atmospheric transmission is monitored by the CSO τ meter, a small dish that performs sky dips to measure τ_{225}, the atmospheric opacity at 225 GHz. These measurements are made once every 15 minutes. We plot atmospheric transmission ($e^{-\tau}$) for 0.5 and 2.0 mm of precipitable water vapour in Figure 2.1. These values correspond to very good weather, $\tau_{225} = 0.03$, and average weather, $\tau_{225} = 0.10$. We see that transmission is significantly lower at 320 GHz, and that we are in fact right on the edge of a strong absorption line. Transmission at 320 GHz is 0.72 ($\tau_{320} = 0.32$) when $\tau_{225} = 0.03$ and 0.48 ($\tau_{320} = 0.74$) when $\tau_{225} = 0.10$.

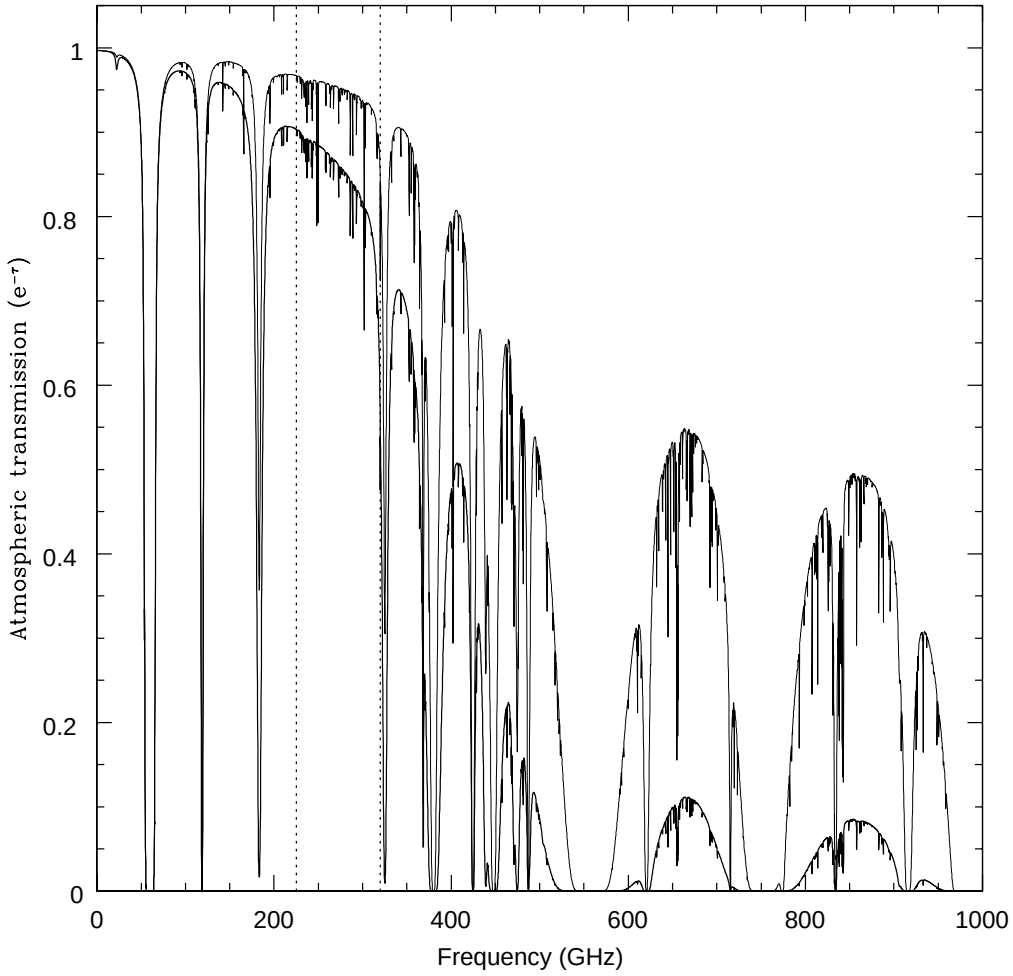

Figure 2.1: Atmospheric transmission as a function of frequency. The upper curve is for 0.5 mm of water vapour ($\tau_{225} = 0.03$), the lower for 2.0 mm ($\tau_{225} = 0.10$). The dotted lines denote the frequencies at which (left) the opacity is measured (225 GHz) and (right) our observations are performed (320 GHz). Note that the observation frequency is right at the edge of a strong absorption line.

2.3 Observing CL 1358+62-G1

F97 find that the Si II emission line from G1 is $\sim 200\,\mathrm{km\,s^{-1}}$ wide. For lack of more information, we make the simple assumption that the [C II] line is also $\sim 200\,\mathrm{km\,s^{-1}}$ wide, corresponding to $\sim$ 200 MHz at our observing frequency. Data from the 50 MHz spectrometer is therefore of little use, since it is narrower than the line. While the 500 MHz detector is wider than the expected line width, it is still too narrow to properly detect the continuum on either side of the line. Consequently, we concentrate our efforts on the 1500 MHz data; we ignore the 50 MHz data, and use the 500 MHz data only for comparison purposes.

We centred the receiver on the nominal line centre, 320.939 GHz, for the first night and shifted by $\Delta v = 129.8\,\mathrm{km\,s^{-1}}$ for nights 2 and 3. This was an attempt to avoid confusing any systematic detector response with the shape of the emission line.

The telescope was pointed at α = 13:59:39.0, δ = 62:30:47. F97 does not give the coordinates of the source, but its position was read off the HST image presented and compared to coordinates of cluster members published by Luppino et al. [27]. This process is accurate to within a few arcseconds, which is well within the CSO beamsize at this frequency ($\simeq 20''$).

The secondary chop throw was set to $60''$ at 1.123 Hz on night 1 and $40''$ at 0.7 Hz on nights 2 and 3. Pointing calibrations were performed occasionally throughout each night, using the ^{12}CO $(3 \rightarrow 2)$ line of IRC 10216. Due to computer malfunctions, the spectrometers had to be restarted several times throughout the observing run. This caused small shifts in the AOS velocity centers and spacings, which complicates the analysis.

The weather during the observing run was very good. The conditions on night 1 were excellent, with $\tau_{225} \sim 0.03 - 0.04$. The weather was not as good on nights 2 and 3, but still above average with $\tau_{225} \sim 0.05 - 0.07$. As noted in Section 2.2, however, the optical depth at 320 GHz is considerably worse than at 225 GHz.

In all, we acquired $\sim$ 450 usable source scans simultaneously in each of the 500 and 1500 MHz detectors. Exact numbers are detailed in Table 2.1.

Table 2.1: Detailing of observations. Row 1 shows the line centre of the receiver on each night. The rest of the table displays the number of scans taken on each night in each detector.

Night:		**1**	**2**	**3**
Receiver centre (GHz):		320.939	320.800	320.800
1500 MHz	No. Source scans:	142	236	42
	No. Cal. scans:	42	71	10
500 MHz	No. Source scans:	142	236	42
	No. Cal. scans:	41	75	10

Chapter 3

Data Reduction

CSO spectroscopic data are usually analyzed using a set of standard procedures provided with CLASS (Continuum Line Analysis Single-dish Software), a software package developed for analysis of continuum line data [6]. Since we are working with very low signal-to-noise data, however, we decided to write our own analysis procedures, both within the CLASS platform and externally in IDL, in order to exert maximum control.

We work with both the 500 and 1500 MHz data. As discussed in Chapter 2, the 500 MHz data is probably too narrow to detect the emission line, but we use it with the 1500 MHz data to help quantify the relative success of our data reduction techniques. Sample source and calibration scans are shown in Figure 3.1. We note that the excess noise at the band edges is due to the 1500 MHz spectrometer bandwidth being wider than the 1 GHz IF signal.

In this chapter, we discuss in detail the data analysis performed. The data reduction presents two primary challenges: how do we decalibrate and combine the data, both within a night and across all three nights? These questions are addressed in what follows.

3.1 Calibration scans

The CSO data acquisition system divides each source scan by the previous calibration scan before writing the data to file. We decided to examine whether this is the best way to use the calibration scans. We recognize that our signal-to-noise is quite low so mis-calibration of single scans might not be a real issue; one might imagine, however, that a certain calibration scan could be noisier than average, and this noise would propagate through to the following source scans. We first examine the 500

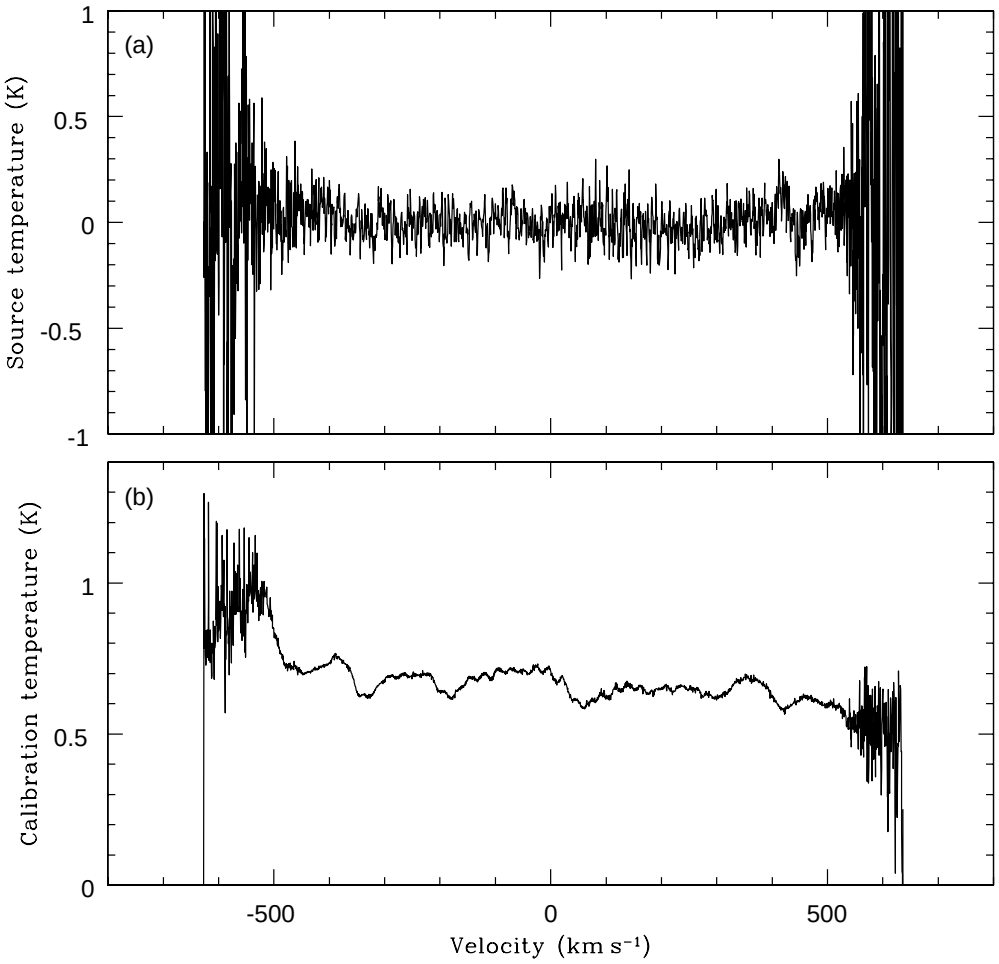

Figure 3.1: Sample raw data, from the 1500 MHz detector. Panel (a) is a typical source scan, and panel (b), a sample calibration scan. The excess noise at the band edges is due the fact that the intermediate frequency (IF) signal output by the local oscillator has 1 GHz bandwidth, smaller than the spectrometer's bandwidth. The 500 MHz scans are similar, except that they do not show the noisy edges, since the spectrometer bandwidth is narrower than the IF signal.

and 1500 MHz calibration scans to see if we can detect any behaviour that would help determine the best way to deal with the calibrations.

3.1.1 Average values

Figure 3.2a shows the average temperature across each good calibration scan, for both the 500 and 1500 MHz detectors. The average value is a good indicator, since the scans are well behaved; they have low noise and common shape. We see a slow drift with occasional jumps in both bands, and note that the 500 and 1500 MHz scans track each other very well, suggesting that the calibration scans are indeed well behaved. The jumps presumably correspond to receiver retunings. There is one section in the middle of night 2 where the 1500 MHz calibration mean jumps and the 500 MHz does not. We are unsure why this happened, and conclude that there was some value in having the 500 MHz data for comparison.

3.1.2 Source scan variance

Figure 3.2b is the variance of the raw source scans. Again, we notice slight drifts in time, with sudden jumps that correspond with the jumps in calibration average. Because our on-source measurements are at a very low level of signal-to-noise, we expect that the data are mostly a measure of the temperature of the sky at the time of observation, as well as the detector systematic response. The calibration scans also measure the sky temperature, but at a different gain. We thus expect the calibrated source spectra to vary less in time than the calibration scans, which appears to be the case.

3.1.3 Atmospheric opacity

Figure 3.2c shows the atmospheric optical depth measured at 225 GHz, as described in Section 2.2. For the most part, the variance and calibration averages correlate well with τ_{225}. Since τ is effectively a measure of the sky temperature and the calibration scans vary with the negative of sky temperature, we expect the calibration mean to vary with $-\tau$. Figure 3.2c shows that this is clearly the case. We are therefore

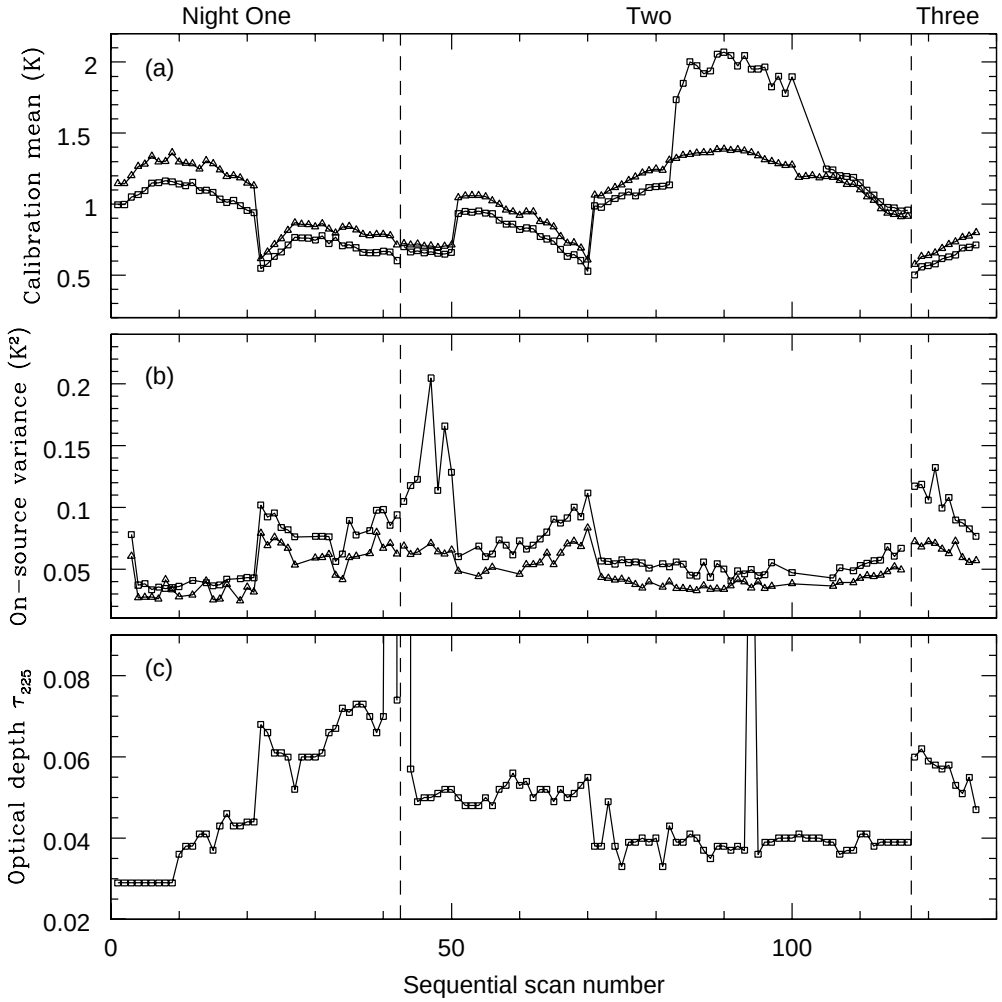

Figure 3.2: Trends in data as a function of time: Panel (a) is the mean value of each calibration scan for both the 1500 MHz (squares) and 500 MHz (triangles) detectors, measured in Kelvin (K). Panel (b) is the variance of the source scans for both detectors, in K^2. Panel (c) is the optical depth measured at 225 GHz with the CSO τ meter. Note the correlation between all three panels. The vertical dashed lines indicate the divisions between the 3 nights.

fairly confident that the system is well behaved and that we understand how the calibration and source scans behave with atmospheric conditions.

3.1.4 Recalibration strategies

We propose three possible methods of calibrating the data:

i) Naively average together all calibration scans within each night, and for each source scan use the appropriate averaged calibration scan.

ii) For each source scan, use the most recent calibration scan: the CSO default.

iii) For each night, interpolate each calibration channel in time.

Each of these possibilities has its advantages and disadvantages. Method (i) will produce the lowest noise calibration scan, but this will poorly reflect the change in atmospheric opacity throughout the night. This method is also complicated by the occasional changes in velocity centre and spacing changes throughout the night (see Section 2.3). Method (ii) is the easiest to implement since it is done by default, but produces the highest noise individual calibration scans. Method (iii) takes into consideration that the atmospheric opacity changes between the times when calibration scans are taken, and will help reduce the effect of the noisiest calibration scans, but there are also a couple of problems with it: interpolating across a gain "jump" would be detrimental, and the method is complicated by limitations of the CLASS software and also the changes in velocity spacing. We thus interpolate over each part of the night where the velocity spacing is unchanged. The limitations of CLASS make it difficult to perform a true interpolation in time, so we instead use an approximation to a spline: for each source scan, we use a 1-2-2-1 weighting of the two preceding and two following calibration scans. At boundaries, where we have one or zero preceding scans, we "reflect" the calibration scans and use the following scans twice, and similarly when missing following scans.

The data are analyzed using all three methods and we compare the variances of the summed scans to see which method results in the lowest noise in the final spectrum.

3.2 Noise analysis

In order to minimize the effect of baseline drift in the detectors, we subtract the baseline (offset) from each source scan. The mean value of a full 1500 MHz scan is noisy, however, because of the excess noise at the band edges. We wish to find a quantitative way to exclude them. We might also wish to exclude the central region from the mean since we expect an emission line would bias the baseline high. However, the signal-to-noise ratio in any one scan is much to small for the line itself to have any effect.

To quantitatively determine where the "noisy" regions of the source scans are, we examine the variance across each scan. We do this by calculating the variance in a 50-channel window centred at each channel in the scan. These curves have a characteristic shape across the entire sample of source scans, so we average together several scans to reduce the noise; we average four randomly chosen source scans with the same velocity axis. In Figure 3.3 we plot the mean inverse variance for seven of these groups of four; three from each of nights 1 and 2, and one from night 3. We note that, as expected from visually inspecting the source scan curve, the edges are very noisy compared to the central regions. Unexpectedly, however, we see that the central $\sim 10^{\text{th}}$ of the scan is slightly noisier than the rest. We use the flattest parts of the scans to calculate the baselines: channels $500 - 1000$ and $1300 - 1700$. The 500 MHz detector does not show such strong features, so we reject only 50 channels from each edge of the source scans, and therefore calculate the baseline on channels $50 - 975$.

3.3 Scan summing

To co-add the data within each night, we perform a weighted average, defined as

$$\tilde{x}_i = \frac{\sum_j w_j x_{ij}}{\sum_j w_j}, \tag{3.1}$$

where $\tilde{x}_i$ is the average of the i^{th} channel of each of the j source scans for each night, x_{ij} is the i^{th} channel of the j^{th} scan, N is the number of scans in the average, and

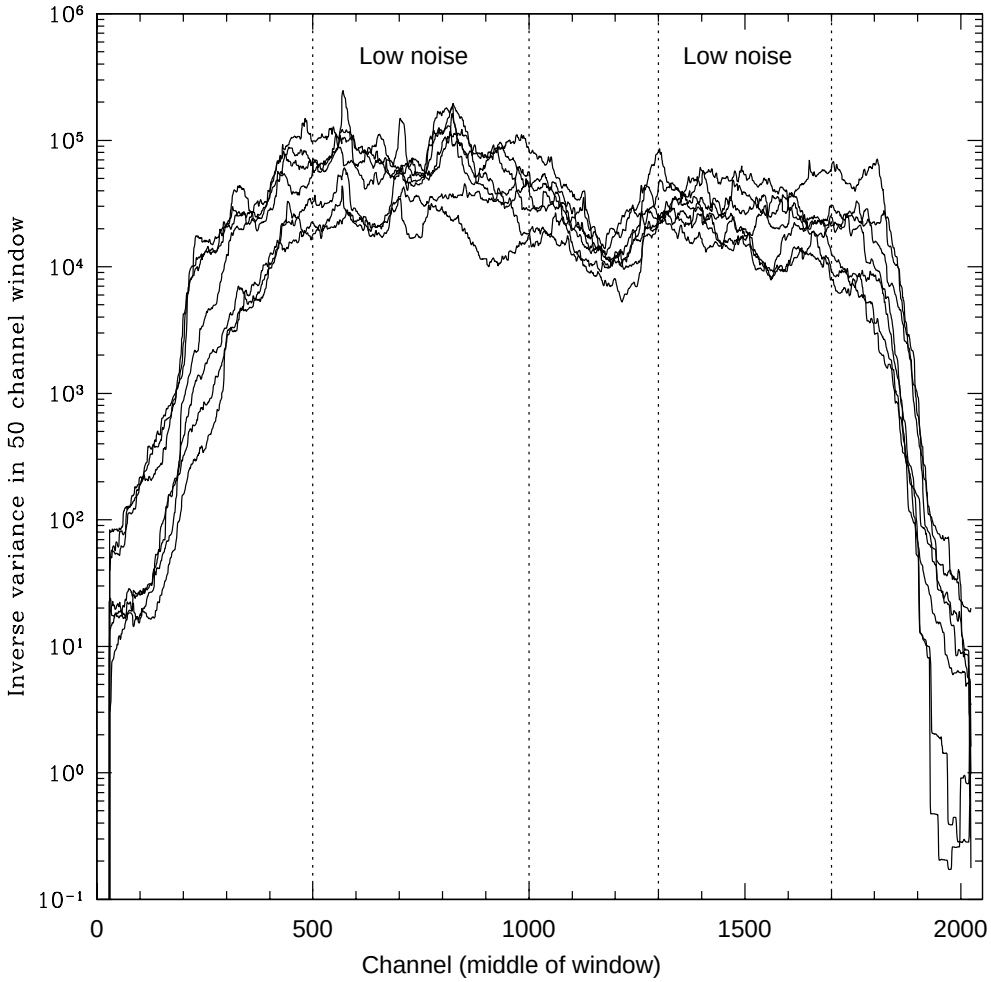

Figure 3.3: The noise as a function of channel in the 1500 MHz source scans. Plotted is the weight (inverse variance) in a 50-channel window across the scan. Each curve is the average weight of 4 randomly chosen source scans, each within the same night with the same velocity spacing. The 500 MHz curves are similar, but without the large features at either edge.

w_j is the weight, calculated as

$$w_j = [\mathrm{var}(x_j)]^{-1} = \left[\frac{1}{N' - 1} \left(\sum_{i'} x_{i'j}^2 - \frac{1}{N'} \left(\sum_{i'} x_{i'j} \right)^2 \right) \right]^{-1} . \qquad (3.2)$$

Here, x_j represents the j^{th} scan and the sums are over the N' channels used in the calculation, as determined in Section 3.2. We perform an average instead of a sum since temperature is equivalent to specific intensity, which is a *per unit time* measurement. Summing the data is essentially multiplying the signal by the observing time, thus we divide the sum by the number of observations.

The summing procedure is complicated by the changes velocity spacing, so we cannot simply average channel by channel. Instead, we interpolate each scan to a common velocity axis. We must be careful, though, since interpolation tends to smooth out the data. Instead of simple linear interpolation (for which this effect will be strongest), we use a cubic spline algorithm [34]. We find that, on average, the RMS of a scan is reduced by 2% by the process of cubic spline interpolation, as opposed to 7% by linear interpolation. The interpolated source scans are co-added, channel by channel as described above.

3.4 Recalibration results

We test the different calibration methods discussed in Section 3.1.4 by examining the RMS variation of the co-added source scans for each of the three nights. See Table 3.1 for results. We note that night 1 is comprised of 142 observations, night 2 of 236, and night 3 of 42. The night 2 results are therefore the most statistically significant. We clearly see that Method (i) is inferior, by a few percent. Whether Method (iii) should be preferred to Method (ii) is less clear — the numbers are consistent with 0% improvement. However, despite the low significance of the difference in RMS, we use Method (iii) to recalibrate the source scans.

Table 3.1: The RMS of the summed source scans (in mK), for each of the three nights using each of the three calibration options (see Section 3.1.4). The percent increase in RMS compared to Method (ii), the default, is listed in parentheses. See Section 3.4.

	Method	**Night 1**	**Night 2**	**Night 3**
1500 MHz	i	4.238 (2.7)	3.090 (0.3)	12.30 (2.3)
	ii	4.125 (0.0)	3.001 (0.0)	12.02 (0.0)
	iii	4.136 (0.3)	3.008 (0.2)	11.85 (-1.4)
500 MHz	i	3.500 (4.2)	2.534 (1.3)	10.09 (2.5)
	ii	3.358 (0.0)	2.501 (0.0)	9.84 (0.0)
	iii	3.374 (0.5)	2.511 (0.4)	9.72 (-1.2)

3.5 Summing nights

We have three co-added scans, one for each night, which we would like to add together. Again, the sum is more complicated than a simple channel by channel weighted sum because of the changes in velocity spacing within each night, in addition to the velocity centre shift between nights 1 and 2. Again, we bin the data to a common velocity axis, making sure to shift nights 2 and 3 by $\Delta v = \frac{\Delta\nu}{\nu_0}c = 129.8\,\mathrm{km\,s^{-1}}$. We average the bins weighted by the variance of the data in each. We choose bins 64 channels wide ($\sim 40\,\mathrm{km\,s^{-1}}$ for the 1500 MHz data), which properly samples the expected width of the emission line ($\sim 200\,\mathrm{km\,s^{-1}}$).

We average, rather than sum, the bins, for the same reason as discussed in Section 3.3. The error bar on the i^{th} bin, $\tilde{\sigma}_i$, is calculated as

$$\tilde{\sigma}_i = \left(\sum_j \frac{1}{\sigma_{ij}^2} \right)^{-\frac{1}{2}}, \tag{3.3}$$

where σ_{ij} is the RMS of the i^{th} bin of the j^{th} night. The size and centres of the bins are varied to ensure our result is not an artifact of the binning. We repeat the analysis with half as many bins (128 channels per bin) and twice as many bins (32 channels per bin), and for each of the three bin sizes, offset the bins by half a

bin. We find no significant difference in our final result due to the choice of binning scheme.

3.6 Converting to flux

Finally, we convert the final co-added spectrum from antenna temperature (K) to flux density (mJy). We use the Rayleigh-Jeans law to convert from temperature T to specific intensity,

$$B_\nu = \frac{2kT\nu^2}{c^2}, \tag{3.4}$$

and then to flux density,

$$S_\nu = B_\nu \Omega, \tag{3.5}$$

where Ω is the solid angle subtended by the CSO beam. In terms of the beam FWHM and efficiency η,

$$\Omega = \frac{\pi\eta}{4\ln 2} \left(\mathrm{FWHM_{beam}}\right)^2. \tag{3.6}$$

From [23], the beam size and efficiency of the 345 GHz receiver are $\mathrm{FWHM_{beam}} = 24.6''$ and $\eta = 74.6\%$. Finally, we calculate frequency ν from velocity v using

$$\nu = \nu_0 \left(1 - \frac{\Delta v}{c}\right), \tag{3.7}$$

where ν_0 is the central frequency, 320.939 GHz, corresponding to $v = 0$. The resulting spectrum is plotted in Figure 3.4. Clearly the variance is much smaller than the structure — we spent too long at these given baselines. Had we known, we could have optimized the observing strategy by, for example, changing the central frequency ν_0 more often.

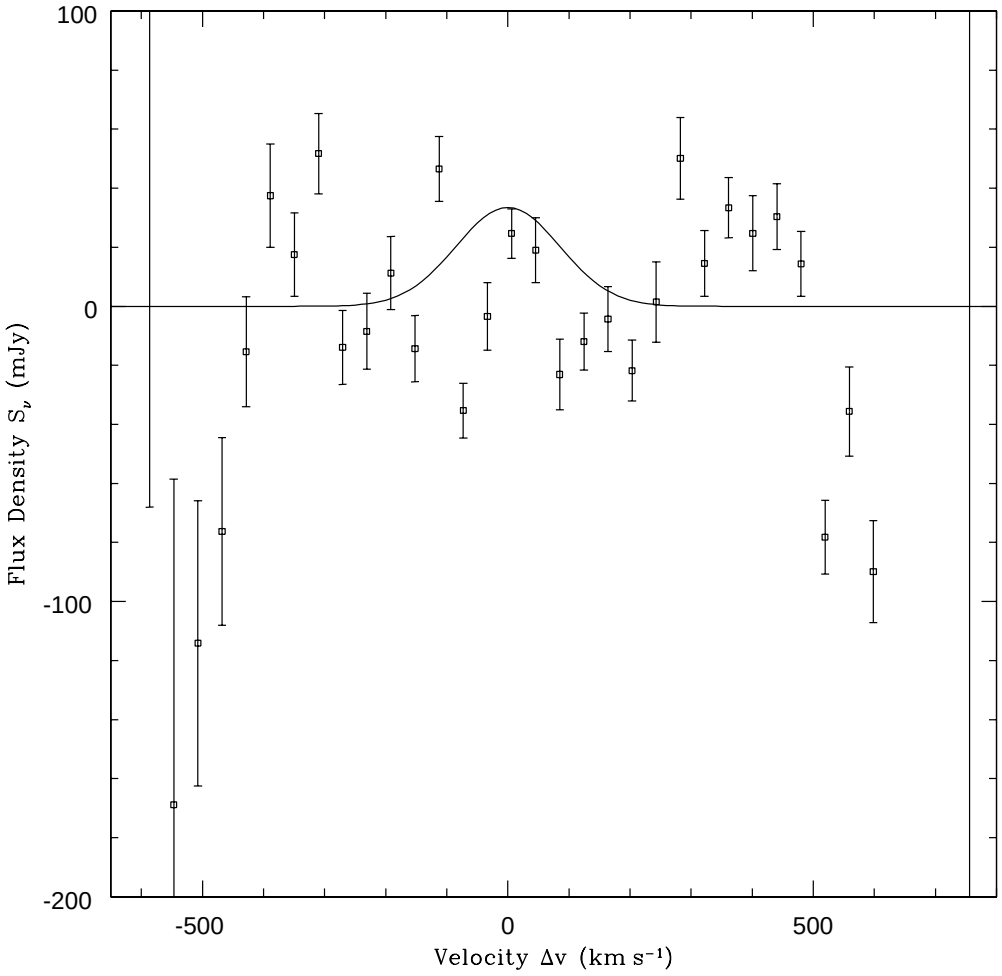

Figure 3.4: The co-added source spectrum, for data from the 1500 MHz detector. Error bars indicate random errors, calculated as the variance of the data in each bin. Clearly the overall scatter exceeds the variance. The solid curve is the 95% upper limit for the [C II] emission line centred at $v = 0\,\mathrm{km\,s^{-1}}$ (320.939 GHz) and with width FWHM $= 200\,\mathrm{km\,s^{-1}}$.

Chapter 4

Interpretation and Results

4.1 Fitting for line strength

Upon visual inspection of the spectrum, it is clear that the data are very noisy. We suggest that we have underestimated our errors, and that there are systematics in the instrument that prevent us from integrating down to such low noise levels. We re-estimate the error bars by finding the best fit Gaussian and scaling the errors so that $\chi^2 \sim N$, and then find an upper limit on the [C II] line strength.

4.1.1 Re-estimating the measurement errors

We fit a Gaussian profile to the spectrum. Because the data are so noisy, a full four-parameter fit will clearly not converge to a useful result. Instead, we fix the baseline, line centre and line width, and fit for line strength. Following F97, we set the line width to $\mathrm{FWHM}_{\mathrm{line}} = 200\,\mathrm{km\,s^{-1}}$, or $\sigma_{\mathrm{line}} = 85\,\mathrm{km\,s^{-1}}$, recalling that $\mathrm{FWHM} = 2\sqrt{2\ln 2}\,\sigma$. We set the line centre v_0 to $0\,\mathrm{km\,s^{-1}}$, since the receiver was centred on 320.939 GHz, [C II] redshifted to $z = 4.9218$; see Chapter 2. The baseline is calculated as the weighted average of all data outside $\pm 2\sigma_{\mathrm{line}}$ of the line centre. We perform a least squares fit to the Gaussian,

$$\tilde{S}_{\nu i}(v_i; S_\nu^0) = S_\nu^0 \exp\left[-\frac{(v_i - v_0)^2}{2\,(\sigma_{\mathrm{line}})^2}\right] + B, \tag{4.1}$$

where S_ν^0 is the line amplitude and B is the baseline, both measured in mJy. We calculate χ^2, defined as

$$\chi^2(S_\nu^0) = \sum_i \left(\frac{S_{\nu i} - \tilde{S}_{\nu i}(v_i; S_\nu^0)}{\sigma_i}\right)^2, \tag{4.2}$$

where $S_{\nu i}$ and σ_i are the flux density and error in bin i. We re-estimate the error bars $\hat{\sigma}_i$ by scaling χ^2 so that $\hat{\chi}^2 = A\chi^2 = N$, the number of bins. This means that

$\hat{\sigma}_i = \sqrt{A}\,\sigma_i$. We find $A = 0.1075$, indicating a very poor fit; the error bars are very likely underestimated. We conclude that the same signal-to-noise could have been reached in far less observing time.

4.1.2 Calculating an upper limit

To determine what our data imply about the strength of the [C II] line, we calculate the likelihood function of the line amplitude,

$$\mathcal{L}(S_\nu^0) \propto \exp\left(-\frac{\chi^2(S_\nu^0)}{2}\right), \tag{4.3}$$

with $\chi^2(S_\nu^0)$ as defined above in Equation 4.2, replacing σ_i by $\hat{\sigma}_i$; see Figure 4.1. We assert the prior $S_\nu^0 > 0$, so that $\mathcal{L}(S_\nu^0) > 0$. The effect of using the re-estimated error bars is to broaden the likelihood curve, $\mathcal{L}(S_\nu^0)$. The most likely line strength, the value of S_ν^0 for which $\mathcal{L}(S_\nu^0)$ is a maximum, is not significantly different from $S_\nu^0 = 0$, so we instead quote an upper limit. This is done by integrating the normalized likelihood function. To find the 95% upper limit, we find the value of $S_\nu^0 = \hat{S}_\nu^0$ for which

$$\frac{\int_0^{\hat{S}_\nu^0} \mathcal{L}(S_\nu^0)\, dS_\nu^0}{\int_0^{\infty} \mathcal{L}(S_\nu^0)\, dS_\nu^0} = 0.95\,. \tag{4.4}$$

We find a 95% upper limit of 33 mJy. This value of S_ν^0 is indicated in Figure 3.4 with a dotted line.

4.1.3 Converting to luminosity

For a given line strength S_ν^0, we can calculate the luminosity in the line, $L_{[\mathrm{C\,II}]}$. First, we integrate S_ν over ν to get total flux S,

$$S = \int S_\nu\, d\nu = S_\nu^0 \sqrt{2\pi}\, \sigma_{\mathrm{line}} = 1.06\, S_\nu^0\, (\mathrm{FWHM}_{\mathrm{line}}), \tag{4.5}$$

where

$$\mathrm{FWHM}_{\mathrm{line}} = \frac{\Delta v}{c}\, \nu_0 \tag{4.6}$$

and $\Delta v = 200\,\mathrm{km\,s^{-1}}$, the full-width half-maximum in velocity space. We then convert to luminosity L by integrating over the sphere centred at the source,

$$L = 4\pi\, D_{\mathrm{L}}^2\, S, \tag{4.7}$$

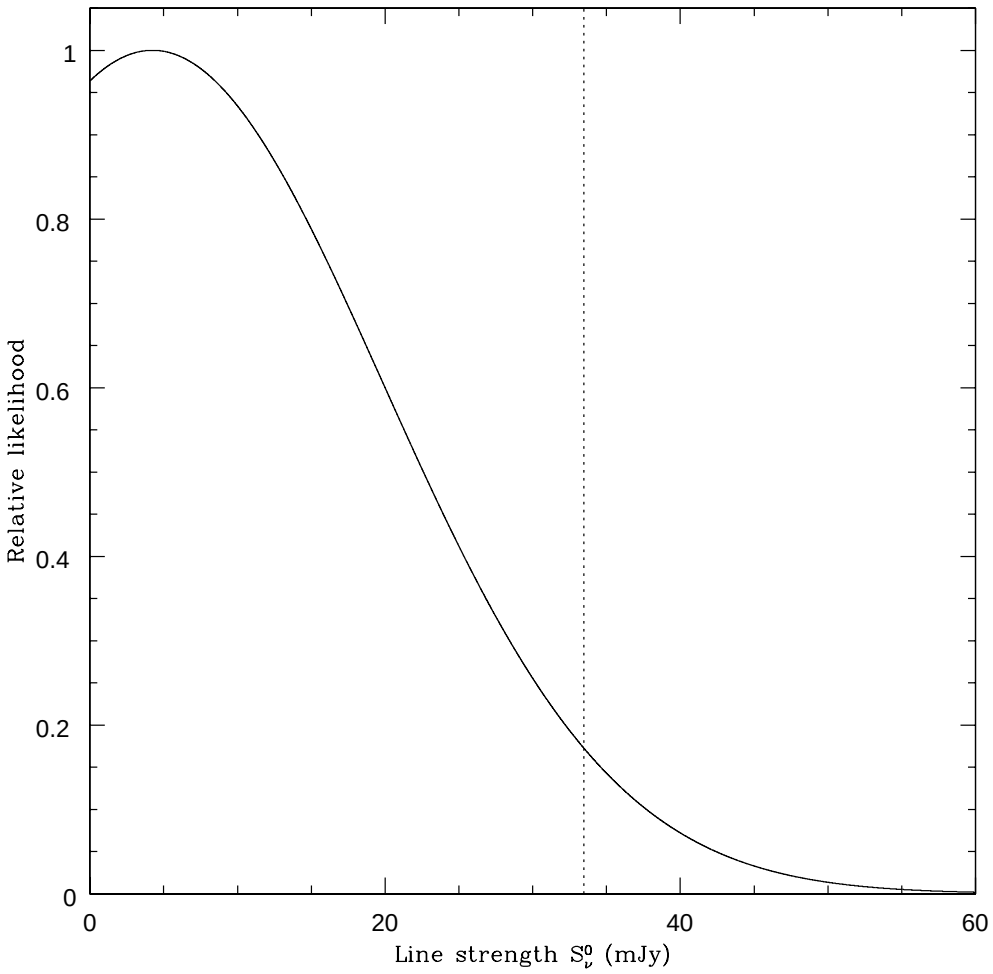

Figure 4.1: The likelihood function for the [C II] luminosity, $\mathcal{L}(L_{[\mathrm{C\,II}]})$. The dotted vertical line indicates the 95% confidence upper limit, $L_{[\mathrm{C\,II}]} \leq 33\,\mathrm{mJy}$.

where $D_{\rm L}$ is the effective "luminosity" distance, dependent on the assumed cosmology. If we take $\Omega_K = 0$,

$$D_{\rm L} = (1+z)\frac{c}{H_0}\int_0^z \frac{dz'}{\sqrt{\Omega_{\rm M}(1+z')^3 + \Omega_\Lambda}}. \tag{4.8}$$

We assume a standard cosmological model with $\Omega_{\rm M} = 0.3$, $\Omega_\Lambda = 0.7$, and $H_0 = 70\,{\rm km\,s^{-1}\,Mpc^{-1}}$ and find $D_{\rm L} = 45.80\,{\rm Gpc}$. The 95% upper limit of $S_\nu = 33\,{\rm mJy}$ calculated in the previous section corresponds to $L_{[{\rm C\,II}]} = 5.4\times10^9\,{\rm L_\odot}$. This calculation does not account for lensing, however; we discuss lensing models in Section 5.1.

Since the conversion from line strength to luminosity is linear in S_ν^0, the likelihood function for [C II] luminosity $\mathcal{L}(L_{[{\rm C\,II}]})$ is a simple rescaling of $\mathcal{L}(S_\nu^0)$, calculated in the previous section. The likelihood of $L_{[{\rm C\,II}]}$ as a function of $\mathcal{L}(S_\nu^0)$ is

$$\mathcal{L}(L_{[{\rm C\,II}]})\,dL_{[{\rm C\,II}]} = \mathcal{L}(S_\nu^0 = L_{[{\rm C\,II}]}/\zeta)\zeta\,dS_\nu^0, \tag{4.9}$$

where ζ is the overall flux density (mJy) $\rightarrow$ luminosity ($\rm L_\odot$) conversion constant ($\zeta = 1.495\ \times\ 10^8\,{\rm L_\odot\,mJy^{-1}}$).

4.2 Far-infrared luminosity

In addition to providing an absolute measurement of the line luminosity, we would like to compare this number to the total luminosity of the object in the FIR. We estimate the FIR luminosity, $L_{\rm FIR}$, by assuming a spectral energy distribution (SED) and scaling it to a narrow-band flux density measurement.

4.2.1 The grey body model

The SED model we use is a modified Plank function, dubbed a "grey body" [7]. This model is a simple approximation to an optically thick black body. The specific intensity is given by

$$(B_\nu)_{\rm grey} \propto \nu^{3+\beta}\left[\exp\left(\frac{h\nu}{kT}\right) - 1\right]^{-1}, \tag{4.10}$$

a Plank function with temperature T multiplied by ν^β. Typical values of the grey body model parameters are $T \sim 40\,{\rm K}$ and $\beta \sim 1.5$ (see discussion by Klaas et al. [22]).

4.2.2 SCUBA measurements

To determine the normalization of the grey body spectrum, we use existing observations in the submillimetre [44]. The object G1 has been observed using the SCUBA instrument on the JCMT at 850 μm, in both photometry and mapping modes. Both sets of data, freely available in the JCMT archives, are combined to produce a beam-convolved map [2]. A roughly 2σ peak is seen within $\sim 2''$ of G1 — since the JCMT beam at 850 μm is $\sim 15''$, we take this peak to be the submillimetre flux from G1. The flux density and noise level at this point are $S_{850} = 2.8$ mJy and $\sigma_{850} = 1.3$ mJy.

4.2.3 Conversion to luminosity

To convert the SCUBA flux measurement to a total FIR luminosity $L_{\rm FIR}$, we first convert the observed frame flux density $S_{\nu(850)}$ to rest-frame luminosity density L_{ν_e} where $\nu_e = (1+z)\nu$ is the emitted frequency which is redshifted to $\nu(\lambda = 850\,\mu{\rm m})$. As with Equation 4.7, we use the luminosity distance $D_{\rm L}$ to calculate L:

$$L_{\nu_e}(S_\nu) = \frac{4\pi\, D_{\rm L}^2}{1+z}\, S_\nu, \tag{4.11}$$

where the extra factor of $(1+z)$ is because the bandwidth of the S_ν measurement is redshifted.

To calculate the total FIR luminosity $L_{\rm FIR}$ we integrate the scaled grey body SED,

$$L_{\rm FIR} = \int L_{\nu_e}(\nu_e)\, d\nu_e, \tag{4.12}$$

where $(L_{\nu_e})_{\rm grey} \propto (B_{\nu_e})_{\rm grey}$ (as given in Equation 4.10), since the conversion factors are independent of ν. We then scale the SED $(L_{\nu_e})_{\rm grey}$ so that $(L_{\nu_e})_{\rm grey} = L_{\nu_e}(S_\nu)$ at $\nu(\lambda = 850\mu{\rm m})$. We find that $S_{850} = 2.8 \pm 1.3$ mJy corresponds to $L_{\rm FIR} = (2.4 \pm 1.2) \times 10^{12}\,{\rm L}_\odot$.

4.2.4 Likelihood function

We take the likelihood function of $L_{\rm FIR}$ to be a Gaussian-distributed random variable with expectation value $\hat{L}_{\rm FIR}$ and width σ_L as determined in the previous section.

We additionally assert that $L_{\rm FIR} \geq 0$,

$$\mathcal{L}(L_{\rm FIR}) \propto \begin{cases} \exp\left[-(L_{\rm FIR} - \hat{L}_{\rm FIR})^2/(2\sigma_L^2)\right] & \text{if } L_{\rm FIR} \geq 0 \\ 0 & \text{otherwise} \end{cases} . \tag{4.13}$$

4.3 [C II] to FIR ratio

We calculate the likelihood of the ratio $L_{\rm [C\,II]}/L_{\rm FIR}$. The combined likelihood for $L_{\rm [C\,II]}$ and $L_{\rm FIR}$ is:

$$\mathcal{L}(L_{\rm [C\,II]}, L_{\rm FIR}) = \mathcal{L}(L_{\rm [C\,II]}) \times \mathcal{L}(L_{\rm FIR}). \tag{4.14}$$

To convert $\mathcal{L}(L_{\rm [C\,II]}, L_{\rm FIR})$ to $\mathcal{L}(L_{\rm [C\,II]}/L_{\rm FIR})$, we first change variables, then marginalize over the nuisance parameter. To simplify notation, we set $x = L_{\rm FIR}$ and $y = L_{\rm [C\,II]}$.

Next, we change coordinates from (x, y) to (ρ, β), where $\rho = \sqrt{x^2 + (ay)^2}$ and $\beta = y/x$ $(= L_{\rm [C\,II]}/L_{\rm FIR})$, and a is a dimensionless parameter chosen so that x and ay are of the same order, which makes the calculations numerically tractable. It follows that:

$$\begin{aligned} x &= \rho/\sqrt{1 + (a\beta)^2} \\ y &= \rho\beta/\sqrt{1 + (a\beta)^2}\,. \end{aligned} \tag{4.15}$$

To convert from $\mathcal{L}(x, y)$ to $\mathcal{L}(\rho, \beta)$, we multiply by the Jacobian, $J(\rho, \beta)$:

$$\mathcal{L}(\rho, \beta) = \mathcal{L}(x, y) \times J(\rho, \beta) \tag{4.16}$$

$$J(\rho, \beta) = \left|\frac{\partial(x, y)}{\partial(\rho, \beta)}\right|. \tag{4.17}$$

We find that $J(\rho, \beta) = \rho\,/\,[1 + (a\beta)^2]$.

Finally, following standard Bayesian analysis procedure [35], we "marginalize over the nuisance parameter", or integrate over ρ,

$$\mathcal{L}(\beta) = \int_0^\infty \mathcal{L}(\rho, \beta)\, d\rho = \frac{1}{1 + (a\beta)^2} \int_0^\infty \mathcal{L}(x, y)\rho\, d\rho, \tag{4.18}$$

where $\mathcal{L}(x, y)$ is evaluated at $(x = (\rho, \beta), y = (\rho, \beta))$ as given in Equation 4.15. The resulting likelihood function $\mathcal{L}(\beta) = \mathcal{L}(L_{\rm [C\,II]}/L_{\rm FIR})$ is plotted in Figure 4.2. Again, the most likely value of β is not significantly different from 0, so we quote an upper limit. To calculate an upper limit we must integrate over β, as in Equation 4.4. We

find, however, that $\int_0^{\beta'} \mathcal{L}(\beta)\, d\beta$ is numerically unstable as $\beta' \to \infty$. We therefore assert the completely reasonable prior $\beta = L_{[\mathrm{C\,II}]}/L_{\mathrm{FIR}} < 1$ and find $\hat{\beta}$ such that

$$\frac{\int_0^{\hat{\beta}} \mathcal{L}(\beta)\, d\beta}{\int_0^1 \mathcal{L}(\beta)\, d\beta} = 0.95. \tag{4.19}$$

We find a 95% upper limit for $\beta = L_{[\mathrm{C\,II}]}/L_{\mathrm{FIR}}$ of 0.4%.

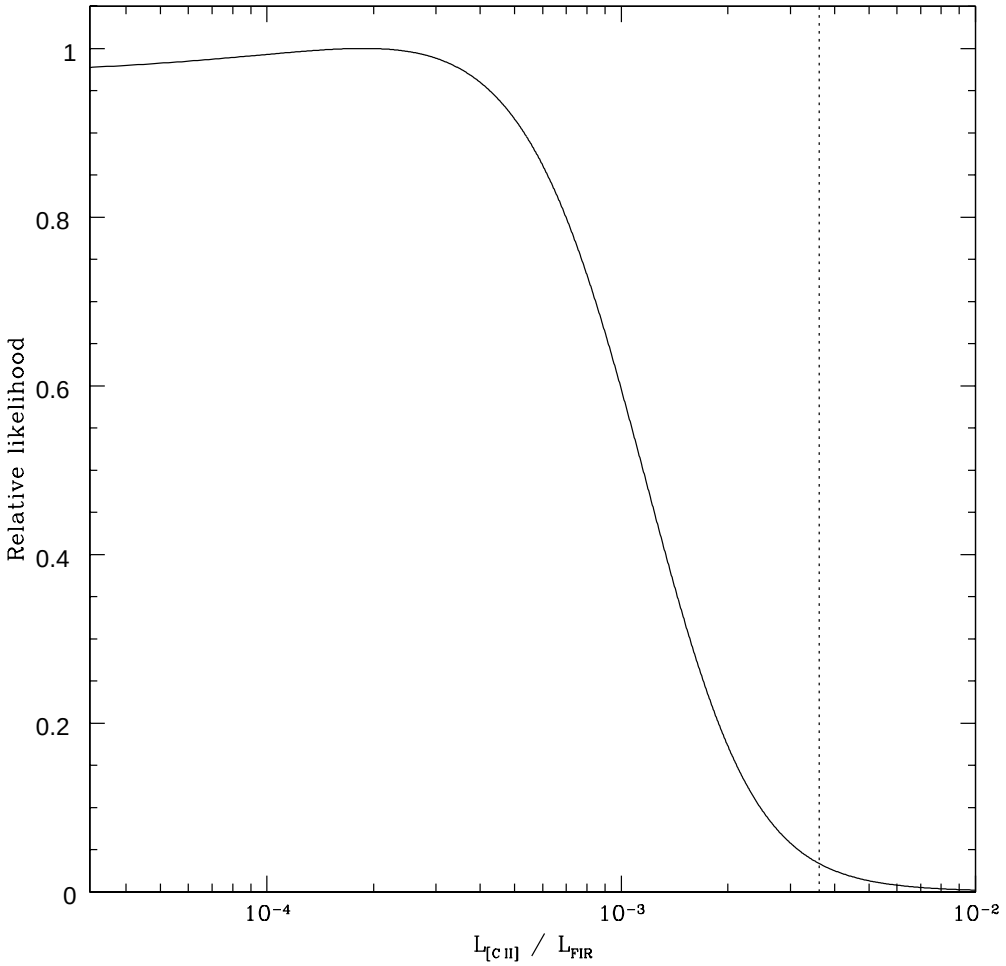

Figure 4.2: The likelihood function for the ratio of [C II] to FIR luminosity, $\mathcal{L}(L_{[\mathrm{C\,II}]}/L_{\mathrm{FIR}})$. The dotted vertical line indicates the 95% confidence upper limit, $L_{[\mathrm{C\,II}]}/L_{\mathrm{FIR}} \leq 0.4\%$.

Chapter 5

Discussion

5.1 CL 1358+62-G1

As discussed in Chapter 1, typical values of $L_{[\mathrm{C\,II}]}/L_{\mathrm{FIR}}$ are thought to be $\sim 0.1-1\%$, but there is recent evidence to suggest that it can be lower, especially for ULIRGs, which are thought to make up some fraction of the high-redshift submillimetre population. We find $L_{[\mathrm{C\,II}]} < 0.4\%\, L_{\mathrm{FIR}}$ at 95% confidence for our particular target. While this does not completely rule out the emission ratios found by S91, it does confine the ratio for this particular high-redshift galaxy to at most the lower end of the range.

F97 determine, based on their lensing model, that the source G1 is magnified by a factor of $5 - 11$. Taking the lower end of this magnification range, we find $L_{[\mathrm{C\,II}]} < 1 \times 10^9\,\mathrm{L}_\odot$. We can use the absolute $L_{[\mathrm{C\,II}]}$ measurement to place an upper limit on the star formation rate (SFR) occurring in the source. Boselli et al. relate SFR to $L_{[\mathrm{C\,II}]}$ by assuming an initial mass function (IMF), with slope $\alpha = 2.35$ and mass cut-offs $M_{\mathrm{up}} = 100\,\mathrm{M}_\odot$ and $M_{\mathrm{low}} = 0.1\,\mathrm{M}_\odot$, and using their [C II] to Hα relation determined from observations of a sample of Virgo galaxies:

$$\mathrm{SFR} = 1.729 \times 10^{-6} \times \left(L_{[\mathrm{C\,II}]}\right)^{0.788}\ \mathrm{M}_\odot\,\mathrm{yr}^{-1}, \tag{5.1}$$

with $L_{[\mathrm{C\,II}]}$ in $\mathrm{L}_\odot$. We naively assume this relation holds for all galaxies at all z, and that the source is not differentially lensed. We find $\mathrm{SFR} \lesssim 16\,\mathrm{M}_\odot\,\mathrm{yr}^{-1}$. As a comparison, F97 find $\mathrm{SFR} \approx 36\,\mathrm{M}_\odot\,\mathrm{yr}^{-1}$, based on near-infrared photometry and the star formation model by Bruzual & Charlot [5]. Hence the SFR implied by our [C II] upper limit is mildly inconsistent with that inferred from the optical. Given the approximations and assumptions made here, though, it is hard to draw any firm conclusions. However, firmer upper limits at these sorts of levels for a sample of

high redshift star-forming galaxies would point to a difference in the role of [C II] in star-forming regions at high redshifts.

5.2 [C II] with future instrumentation

In the near future, several new instruments with increased sensitivity to the submillimetre and millimetre will become available. In particular, the Atacama Large Millimeter Array (ALMA; see [47]) will be ideally suited to measure the [C II] emission line in high redshift sources. It will be a 64-element interferometer of 12-m dishes at Llano de Chajnantor, Chile, functioning in all atmospheric windows between 350 μm and 10 mm. Many authors have estimated the [C II] detection efficiencies for ALMA and other future instruments.

Stark estimates a [C II] luminosity and describes what could be done on a 10 metre antenna at the South Pole [39]. He assumes the [C II] luminosity function has the same form as the Schechter function for galactic luminosity and scales it to $L_{[\mathrm{C\,II}]} \simeq 0.002 L_{\mathrm{gal}}$, based on S91, and that it holds for all z. He then calculates that a 10 m antenna at the South Pole could detect [C II] in a source at $z = 2.2$ or $z = 4.4$, where [C II] is redshifted to peaks of atmospheric windows, in less than 1 hour. He also estimates that a blank field search conducted on the same telescope with a 20 pixel array receiver could produce $\sim$ 1 detection per day. Finally, he suggests that it might be more efficient to search for the redshifted 100 μm dust peak using bolometric photometer arrays at $\lambda = 200$, 300, and 450 μm (see BLAST [12] and Herschel/SPIRE [13]), then verify the redshift of the candidate objects with a line receiver.

Loeb suggests that the [C II] emission line can be used to detect proto-quasars at $z \gtrsim 10$, where the line is redshifted to the millimetre [25]. He optimistically predicts that ALMA will be able to detect a $z \sim 10$ quasar at the 3σ level in 40 minutes. For reasonable assumptions of cosmology and source number density, he predicts that blank sky searches will discover [C II] sources at a rate of $\sim 0.1\,\mathrm{hr}^{-1}$. Suginohara et al. also estimate ALMA's detection efficiency for fine structure lines in $z \gtrsim 10$ galaxies [40]. However, they find the much more conservative integration

time of $\sim 1-2$ weeks for a 3σ detection.

Blain et al. (hereafter B00) give a survey of emission-line searches with upcoming instrumentation [1], which we summarize here. They estimate source counts of molecular and atomic emission lines, including [C II], based on the results of submillimetre-wave continuum surveys.

ALMA B00 predict that the 230 GHz receiver, with a 16 GHz bandwidth, will provide a detection rate of $\sim 15\,\mathrm{hr}^{-1}$. [C II] emission from $z \sim 7$ sources is redshifted into this band.

SPIFI The South Pole Imaging Fabry-Perot Interferometer (SPIFI) is a 5×5 element Fabry-Perot interferometer operating at 460 to 1500 GHz with 8 GHz bandwidth, for use on both the 1.7 m AST-RO at the South Pole and the 15 m JCMT [41]. B00 predict that SPIFI on the JCMT will detect [C II] sources at $z \sim 2$ at a rate of $0.0025\,\mathrm{hr}^{-1}$.

HIFI The Heterodyne Instrument for the Far Infrared (HIFI), one of the instruments planned for use on the 2.5 m Herschel satellite, is a submillimetre spectrometer which will operate at 500 to 1100 GHz, with 4 GHz bandwidth [11]. Galaxies at $z \sim 2$ will be detected in [C II] at a rate of $6 \times 10^{-3}\,\mathrm{hr}^{-1}$.

SPECS The Submillimeter Probe of the Evolution of Cosmic Structure (SPECS) is a proposed far-infrared interferometer, with three 3 m dishes and a 1 km maximum baseline [30]. A 650 GHz detector with 8 GHz bandwidth could detect $z \sim 2$ galaxies at a rate of $0.2\,\mathrm{hr}^{-1}$.

We see that while all of these telescopes will be able to detect [C II] in blank field searches, only ALMA will be able to do it efficiently. The other instruments are most likely better suited for targeted observations, where the redshift is already known.

B00 also discuss telescopes such as the centimetre wavelength Green Bank Telescope (GBT) which will detect CO lines, but are unsuitable for [C II]. The 100 m GBT is currently operational, and with a bandwidth of 3.2 GHz is wide enough to detect at least one CO line from a given high redshift galaxy. Additionally, there are

plans of ~ 35 GHz spectrometers for both the CSO and the 50 m Large Millimeter Telescope (LMT).

5.3 Conclusions

We have observed a high-redshift lensed galaxy at the wavelength of [C II] using the Caltech Submillimeter Observatory. We presented a careful analysis of the data, but did not detect the line emission. We place a 95% upper limit of $L_{[\mathrm{C\,II}]} < 1 \times 10^9\,\mathrm{L}_\odot$ on the lens-corrected luminosity. Using submillimetre continuum observations from SCUBA on the James Clerk Maxwell Telescope, we place a 95% upper limit on the line to continuum ratio of $L_{[\mathrm{C\,II}]}/L_{\mathrm{FIR}} < 4 \times 10^{-3}$.

Bibliography

[1] A. W. Blain, D. T. Frayer, J. J. Bock, and N. Z. Scoville. Millimetre/submillimetre-wave emission-line searches for high-redshift galaxies. *MNRAS*, 313:559, 2000. *B00* in this paper.

[2] C. Borys and S. C. Chapman. Private communication, 2002.

[3] A. Boselli, G. Gavazzi, J. Lequeux, and D. Pierini. [C II] at 158 μm as a star formation tracer in late-type galaxies. *A&A*, 385:454, 2002.

[4] J. Braine, D. Downes, and S. Guilloteau. No CO emission from damped Lyman-α absorbers. *A&A*, 309:L43, 1996.

[5] G. Bruzual A. and S. Charlot. Spectral evolution of stellar populations using isochrone synthesis. *ApJ*, 405:538, 1993.

[6] G. Buisson, L. Desbats, G. Duvert, T. Forveille, R. Gras, S. Guilloteau, R. Lucas, and P. Valiron. CLASS: Continuum line analysis single-dish software. http://iram.fr/GS/class/class.html, 1995.

[7] F. Combes. Gas and dust in protogalaxies. *Ap&SS*, 269:405, 1999.

[8] A. Contursi, M. J. Kaufman, G. Helou, D. J. Hollenbach, J. Brauher, G. J. Stacey, D. A. Dale, S. Malhotra, M. Rubio, R. H. Rubin, and S. D. Lord. ISO LWS observations of the two nearby spiral galaxies NGC 6946 and NGC 1313. *AJ*, 124:751, 2002.

[9] M. K. Crawford, R. Genzel, C. H. Townes, and D. M. Watson. Far-infrared spectroscopy of galaxies: The 158 micron C^+ line and the energy balance of molecular clouds. *ApJ*, 291:755, 1985.

[10] A. Dalgarno and R. McCray. Heating and ionization of H I regions. *ARA&A*, 10:375, 1972.

[11] T. de Graauw, N. D. Whyborn, H. van de Stadt, G. Beaudin, D. A. Beintema, V. Belitsky, P. Cais, E. Caux, M. Gheudin, A. Cros, P. de Groene, A. Emrich, N. R. Erickson, T. C. Gaier, and J. D. Gallego-Puyol. Heterodyne instrument for FIRST (HIFI): Preliminary design. In T. G. Phillips, editor, *Proc. SPIE Vol. 3357: Advanced Technology MMW, Radio, and Terahertz Telescopes*, page 336, 1998.

[12] M. Devlin. BLAST - a balloon-borne large aperture submillimeter telescope. In J. D. Lowenthal and D. H. Hughes, editors, *Deep Millimeter Surveys: Implications for Galaxy Formation and Evolution*, page 59, 2001.

[13] M. W. Griffin et al. SPIRE proposal document. http://www.ssd.rl.ac.uk/spire, 1998.

[14] M. Franx, G. D. Illingworth, D. Kelson, P. G. van Dokkum, and K. Tran. A pair of lensed galaxies at $z = 4.92$ in the field of CL 1358+62. *ApJ*, 486:L75, 1997. *F97* in this paper.

[15] D. T. Frayer. CO and near-infrared observations of high-redshift submillimeter galaxies. In J. D. Lowenthal and D. H. Hughes, editors, *Deep Millimeter Surveys: Implications for Galaxy Formation and Evolution*, page 117, 2001.

[16] D. T. Frayer, R. L. Brown, and P. A. Vanden Bout. CO emission from the $z = 3.137$ damped Lyα system toward PC 1643+4631A. *ApJ*, 433:L5, 1994.

[17] M. Giavalisco. Lyman-break galaxies. *ARA&A*, 40:579, 2002.

[18] D. J. Hollenbach, T. Takahashi, and A. G. G. M. Tielens. Low density photodissociation regions. *ApJ*, 377:192, 1991.

[19] K. G. Isaak, R. G. McMahon, R. E. Hills, and S. Withington. Observations of high-redshift objects at submillimetre wavelengths. *MNRAS*, 269:L28, 1994.

[20] R. J. Ivison, A. P. Harrison, and I. M. Coulson. No C^+ emission from the $z = 3.137$ damped Lyman-α absorber towards PC 1643+4631A. *A&A*, 330:443, 1998.

[21] M. J. Kaufman, M. G. Wolfire, D. J. Hollenbach, and M. L. Luhman. Far-infrared and submillimeter emission from Galactic and extragalactic photodissociation regions. *ApJ*, 527:795, 1999.

[22] U. Klaas, M. Haas, S. A. H. Müller, R. Chini, B. Schulz, I. Coulson, H. Hippelein, K. Wilke, M. Albrecht, and D. Lemke. Infrared to millimetre photometry of ultra-luminous IR galaxies: New evidence favouring a 3-stage dust model. *A&A*, 379:823, 2001.

[23] J. W. Kooi. CSO heterodyne receiver beam efficiency measurements on Mars. http://www.submm.caltech.edu/cso/receivers/beams.html, 2001.

[24] K. J. Leech, H. J. Völk, I. Heinrichsen, H. Hippelein, L. Metcalfe, D. Pierini, C. C. Popescu, R. J. Tuffs, and C. Xu. [C II] 158-μm observations of a sample of late-type galaxies from the Virgo cluster. *MNRAS*, 310:317, 1999.

[25] A. Loeb. Finding protoquasars at high redshifts. *ApJ*, 404:L37, 1993.

[26] M. L. Luhman, S. Satyapal, J. Fischer, M. G. Wolfire, P. Cox, S. D. Lord, H. A. Smith, G. J. Stacey, and S. J. Unger. *Infrared Space Observatory* measurements of a [C II] 158 micron line deficit in ultraluminous infrared galaxies. *ApJ*, 504:L11, 1998.

[27] G. A. Luppino, B. A. Cooke, I. M. McHardy, and C. R. Ricker. Cl 1358+6245 at $z = 0.32$: An X-ray selected, distant, rich cluster of galaxies. *AJ*, 102:1, 1991.

[28] S. C. Madden, A. Poglitsch, N. Geis, G. J. Stacey, and C. H. Townes. [C II] 158 micron observations of IC 10: Evidence for hidden molecular hydrogen in irregular galaxies. *ApJ*, 483:200, 1997.

[29] S. Malhotra, G. Helou, G. Stacey, D. Hollenbach, S. Lord, C. A. Beichman, H. Dinerstein, D. A. Hunter, K. Y. Lo, N. Y. Lu, R. H. Rubin, N. Sibermann,

H. A. Thronson Jr., and M. W. Werner. Infrared Space Observatory measurements of [C II] line variations in galaxies. *ApJ*, 491:L27, 1997.

[30] J. C. Mather, S. H. Moseley, Jr., D. Leisawitz, E. Dwek, P. Hacking, Martin Harwit, L. G. Mundy, R. F. Muchotzky, D. Neufeld, D. Spergel, and E. L. Wright. The submillimeter frontier: A space science imperative. astro-ph/9812454, 1998.

[31] K. Mizutani, T. Maihara, H. Matsuhara, T. Nakagawa, H. Shibai, H. Okuda, Y. Kobayashi, N. Hiromoto, T. Nishimura, and F. J. Low. [C II] 158 micron and [O I] 63 micron observations of the Galactic center region. *ApJS*, 91:613, 1994.

[32] K. Mochizuki. Far-infrared [CII]/continuum ratio toward the central kiloparsecs of M31. *A&A*, 363:1123, 2000.

[33] T. Nikola, R. Genzel, F. Herrmann, S. C. Madden, A. Poglitsch, N. Geis, C. H. Townes, and G. J. Stacey. [C II] emission from NGC 4038/9 (the "Antennae"). *ApJ*, 504:749, 1998.

[34] W. H. Press, S. A. Teukolsky, W. T. Vetterling, and B. P. Flannery. *Numerical Recipes in C.* Cambridge University Press, Second edition, 1992.

[35] D. S. Savia. *Data Analysis: A Bayesian Tutorial.* Oxford University Press, 1996.

[36] B. J. Smith and S. C. Madden. Interstellar gas in low mass Virgo cluster spiral galaxies. *AJ*, 114:138, 1997.

[37] B. T. Soifer. (CII) 158 micrometers observations of the $z = 2.286$ IRAS source FSC10214+4724. Technical Report, California Inst. of Tech., 1996.

[38] G. J. Stacey, N. Geis, R. Genzel, J. B. Lugten, A. Poglitsch, A. Sternberg, and C. H. Townes. The 158 micron [C II] line: A measure of global star formation activity in galaxies. *ApJ*, 373:423, 1991. *S91* in this paper.

[39] A. A. Stark. Potential measurement of the luminosity function of 158 micron [C II] at high redshifts: A test of galaxy formation models. *ApJ*, 481:587, 1997.

[40] M. Suginohara, T. Suginohara, and D. N. Spergel. Detecting $z > 10$ objects through carbon, nitrogen, and oxygen emission lines. *ApJ*, 512:547, 1999.

[41] M. R. Swain, C. M. Bradford, G. J. Stacey, A. D. Bolatto, J. M. Jackson, M. L. Savage, and J. A. Davidson. Design of the South Pole imaging Fabry-Perot interferometer (SPIFI). In A. M. Fowler, editor, *Proc. SPIE Vol. 3354: Infrared Astronomical Instrumentation*, page 480, 1998.

[42] A. G. G. M. Tielens and D. Hollenbach. Photodissociation regions. I. basic model. *ApJ*, 291:722, 1985.

[43] P. P. van der Werf. Observations and diagnostic use of highly redshifted fine structure lines. In C. L. Carilli, S. J. E. Radford, K. M. Menten, and G. I. Langston, editors, *Highly Redshifted Radio Lines, ASP Conf. Series Vol. 156*, page 91, 1999.

[44] P. P. van der Werf, K. K. Knudsen, I. Labbé, and M. Franx. Can dusty Lyman break galaxies produce the submillimetre counts and background? Lessons from lensed Lyman break galaxies. In J. D. Lowenthal and D. H. Hughes, editors, *Deep Millimeter Surveys: Implications for Galaxy Formation and Evolution*, page 103, 2001.

[45] M. White, D. Scott, and J. Silk. Anisotropies in the cosmic microwave background. *ARA&A*, 32:319, 1994.

[46] M. G. Wolfire, A. G. G. M. Tielens, and D. Hollenbach. Physical conditions in photodissociation regions - application to galactic nuclei. *ApJ*, 358:116, 1990.

[47] A. Wootten. Science with the Atacama Large Millimeter Array. In A. Wootten, editor, *Science with the Atacama Large Millimeter Array, ASP Conference Proceeding Vol. 235*, 2001.

[48] E. L. Wright, J. C. Mather, C. L. Bennet, E. S. Cheng, R. A. Shafer, D. J. Fixsen, R. E. Eplee, Jr., R. B. Isaacman, S. M. Read, N. W. Boggess, S. Gulkis,

M. G. Hauser, M. Janssen, T. Kelsall, P. M. Lubin, S. S. Meyer, S. H. Moseley, Jr., T. L. Murdock, R. F. Silverberg, G. F. Smoot, R. Weiss, and D. T. Wilkinson. Preliminary spectral observations of the Galaxy with a 7° beam by the Cosmic Background Explorer (COBE). *ApJ*, 381:200, 1991.